Controlled disturbed flows on the endothelium result in increased inflammation, nuclear lamin disruption and heterochromatin condensation

Neha Paddillaya[1], Suyog Mahulkar[2], Jaywant H Arakeri[2], Namrata Gundiah[2*]

[1]Centre for Biosystems Science and Engineering,

[2]Department of Mechanical Engineering,

Indian Institute of Science, Bangalore, India.

** For correspondence:*

Namrata Gundiah

Biomechanics Laboratory,

Mechanical Engineering department,

Indian Institute of Science, Bangalore 560012.

Email: namrata@iisc.ac.in; ngundiah@gmail.com

Tel: 91 80 2293 2860/ 3366

Short title: Secondary flow effects on endothelial monolayers in novel microfluidic device

Abstract

Early atherosclerotic lesions often develop in arterial bifurcations and curvatures that experience complex disturbed flows. Lab-on-chip devices primarily adopt laminar unidirectional and oscillatory flows to characterize endothelial mechanobiology and test therapeutics. Such flows do not reproduce the time-varying, bidirectional, and complicated shear patterns on arterial walls. We fabricated an endothelium-on-chip device and developed a semi-analytical model to produce any prescribed wall shear pattern characterized by a shear rosette. We quantified responses of Human Aortic Endothelial Cell (HAEC) monolayers subjected to unidirectional laminar (Uni-L) and oscillatory (Uni-O) flows in straight microfluidic channels, and a circular shear rosette (Bi-O), defined by bidirectional oscillatory flows, in the new device. Immunofluorescence results show well-defined stress fibers and VE-cadherin under laminar flows. Cells were more cuboidal with significantly larger nuclear areas in the device as compared to other groups. Lamin A/C disruption and heterochromatin reorganization were evident in nuclei of cells in the Bi-O group but were absent in the Uni-L and No-flow control groups. Cells showed significantly elevated actin, VE-cadherin, inflammatory NF-kB, and lamin expressions in the device compared to other groups. A device to create controlled disturbed flows offers a platform to assess mechanobiology, has significant potential in personalized medicine, and reduces reliance on animal trials.

Endothelial cells (EC) line the blood vessel lumen and are subjected to cyclically varying and complex shear stresses due to the fluid flow. Wall shear stress (WSS) activates multiple signal transduction pathways through adhesive proteins that link the EC monolayer to the underlying matrix, cytoskeletal proteins, caveolae, tyrosine kinase receptors, ion channels, the glycocalyx, and primary cilia[1]. Response of the endothelium to mechanical stimuli is important in angiogenesis[2], vascular remodeling[3], and chronic inflammatory arterial diseases, including atherosclerosis[4]. Straight sections of small arteries and capillaries generally experience laminar shear stresses, whereas branch points, regions downstream of curved sections, and bifurcations are subjected to more complex stresses during normal cardiac activity (Fig. 1a, b). Early atherosclerotic lesions develop along curved regions and in arterial bifurcations[5,6]. Macrophages localize below the endothelium in regions of lower curvature in the murine aortic arch and at branch points of large arteries[7]. Higher atherosclerotic expression in regions experiencing disturbed flows correlates with changes in WSS magnitude and direction[8,9]. Complex flows activate and upregulate endothelial NO synthase (eNOS) *via* inflammatory signaling due to NF-kB[7–10]. Increased nitrous oxide (NO) results in higher expression of leukocyte adhesion molecules, including VCAM-1 and E-selectin, that promote the diseased phenotype[7].

Physiological arterial flows are significantly more complex than laminar and oscillatory flows due to unsteady or pulsatile and spatially developing conditions[11,12]. High wall curvature in the ascending aorta and smaller cerebral arteries leads to the generation of secondary flows caused by an imbalance between centrifugal forces and the radial pressure gradient[13]. Interactions between unsteadiness and curvature are highly nonlinear and result in flow separations and reversals, vortical structures, and regions of WSS stagnation/ fixed points– these are broadly labeled as “disturbed” flows[13]. Devices based on microscale technologies use laminar unidirectional or oscillatory flows in straight microfluidic channels to assess changes

in endothelial mechanobiology[8,14,15,16,17]. Generating *controlled* disturbed flows, similar to those found in disease prone arterial regions, has, however, been a challenge to implement in lab-on-chip devices. Whereas steady laminar channel flow past a ridge/ obstruction produces a separated flow in the wake, no secondary flows are generated [18–20]. Alternate methods, such as orbital shaker, generate complex multidirectional shear stresses that can be applied to EC monolayers[21]. This method is, however, not capable of creating specified and controlled temporal variations in WSS.

We recently proposed a graphical method to characterize the temporal changes in flow dynamics at each point of the arterial wall. This method uses variations in the WSS vector along the principal and orthogonal flow directions, and represents them as a polar "shear rosette" plot[11] The rosette size is a measure of the WSS magnitude, variations about the centroid indicate oscillations, and shape deviations from linearity signify the extent of flow bidirectionality[11]. Ratio of the rosette width to length, defined as anisotropy ratio (AR), is a useful method to quantify secondary flows. Regions with high AR values (~1), such as the inner curvature of ascending aorta and arterial bifurcations, exhibit strong secondary flows, whereas those with AR=0, such as straight sections of arteries, experience laminar unidirectional flows. The AR serves as a useful metric to quantify the presence and strength of secondary flows in arteries.

In this work, we report the development of a novel microfluidic device that utilizes two synchronized syringe pumps to generate any arbitrary shear rosette shape at the device centroid. To achieve this, we developed a semi-analytical model to calculate input flow rate variations to each pump. We validated the model accuracy for various rosette shapes using computational fluid dynamics (CFD) and experimental flow visualization. We studied changes in cellular and nuclear mechanobiology using human aortic endothelial cell (HAEC) monolayers subjected to a circular shear rosette, characterized by bidirectional oscillatory flows, in the device. We

compared these results with cells exposed to laminar and oscillatory unidirectional flows in straight microfluidic channels with No-flow control. PCR studies show several fold changes in inflammatory NF-kB, VE-cadherin, and lamin A/C markers. Elucidating the mechanisms underlying EC responses to controlled disturbed flows is essential to our understanding of factors that may be involved in the pathophysiology of vascular disease, developing patient specific therapeutics to modulate EC behaviors, assessing bacterial/ viral interactions with EC, and characterizing thrombus formation.

Results

Generation of "controlled" disturbed flows using microfluidics

We fabricated the endothelium-on-chip device using replica molding with PDMS (Fig. 1 c). The device consists of three arms with an angular separation of 120º (Fig. 1c). Two of these arms are connected to synchronized syringe pumps that serve as inlet ports, whereas the third arm serves as a reservoir port. We adjusted the input flow rates to the two pumps using the semi-analytical model (see Methods) to achieve any desired shear rosette pattern at the device centroid. For a physiological WSS magnitude of 1Pa[11], the inlet flow velocities required to generate a circular rosette at the device centroid (Fig. 1d) are given by

$$V_1 = 0.0579\sin(2\pi t + 0.492) \quad and \quad V_2 = 0.0579\sin(2\pi t + 2.649) \qquad (1)$$

These expressions are different for other rosette shapes. We validated this approach with CFD implemented using ANSYS-Fluent (Fig. S1, Fig. S2, Table T1, and Table T2). Velocities from Equation 1 were used at the pump inlets, and the corresponding WSS variations were calculated (Fig. 1e; Movie 1). Fig. 1d shows a significant overlap between rosette shapes from CFD simulations with the targeted circular rosette at the device centroid. We computed the Anisotropy Ratio (AR)[11] at each point in the device using temporal variations in WSS. Fig. 1f shows a contour plot that shows radially varying AR with distance from the device centroid.

Regions close to the inlets and the reservoir have WSS regions characterized by AR=0 due to the unidirectional oscillatory flow.

The semi-analytical model is useful to generate any arbitrary shear rosette shape that describes disturbed flows. Fig. 1g shows replication of the rosette for diseased aneurysmal inner carotid artery (ICA) at the device centroid with model calculations[11] obtained using inlet velocities in Fig. 1h. The peak AR values (=0.45), shown as a contour map in Fig. 1i, are off-centered from the centroid. Movie 2 shows time variations in the inlet pumps that produce the targeted rosette for ICA. We replicate a few other conditions, such as an elliptical (Fig. S3a) and a complex rosette (Fig. S3d) reported in an aneurysmal ascending aorta, using this method[21]. To experimentally confirm these results, we performed flow visualization using fluorescent microspheres as tracer particles (Movie 3). The tracer particle streak images, obtained with long exposure, show flow streamlines within the channel. A comparison between streamlines obtained from CFD studies and streak images of flow visualization experiments is shown at two time points for a circular rosette (Figs. 1k, 1m; Figs. 1j, l). Streamlines patterns show a good match with those obtained using CFD calculations. The semi-analytical model hence serves as a robust approach to generate arbitrary shear rosette conditions that characterize disturbed flows. This method represents the first successful demonstration of producing controlled disturbed flows in micro-fluidic devices[23].

Endothelial cells are enlarged and rounded under bidirectional oscillatory flows

Endothelial cell shapes have been causally linked to increased atherogenic gene expression and inflammation that lead to plaque formation[8,24]. EC morphologies are spindle shaped and align in the flow direction under laminar and unidirectional conditions in contrast to atheroprone regions that have rounded cells[8,25,26]. How do bidirectional oscillatory flows influence endothelial cellular and nuclear morphologies? We cultured HAEC monolayer on a collagen-1 coated coverslip and clamped the replica molded PDMS device to the cell-coated

substrate (see Methods). We included inlets to the pumps and a reservoir to create the endothelium-on-chip device[23]. This method significantly reduces the time required to grow EC monolayers in microfluidic devices and minimizes the media used to achieve cell confluency prior to flow experiments.

We subjected the HAEC monolayer to a circular shear rosette (Bi-O) in the device for 24 hours. Cells were fixed and stained at the end of the experiment with Rhodamine Phalloidin to visualize actin (red) and DAPI to label the nuclei (blue). Cell boundaries and nuclei were segmented using the TissueAnalyser plugin in Fiji (ImageJ), and their areas and aspect ratios were calculated (~300 cells). Results from the Bi-O condition were compared with corresponding parameters for EC monolayers in straight channels subjected to unidirectional laminar (Uni-L) and oscillatory (Uni-O) flows. Cells on collagen-1 coated coverslips without flow were used as a control in the study (No-flow).

Fig. 2a shows representative immunofluorescence images of HAEC monolayers for the various flow conditions. Laminar flows resulted in highly elongated cells along the flow direction. Cell shapes were significantly altered under oscillatory flows with higher actin intensities. HAECs in the Uni-O group had the lowest cell areas (996.92±131.78 μm^2) and aspect ratios (2.01±0.73) compared to the Uni-L group that had the highest areas (3491.60±655.90 μm^2) and aspect ratios (8.63±2.64) (Fig. 2c,d). Areas for the No-flow group (1642.80±155.23 μm^2) lie between these values; the corresponding aspect ratios (2.67±0.75) were not significantly different from the Uni-O group (Fig. 2c,d). The Bi-O group had cuboidal cells with significantly greater areas (2177.12±270.34 μm^2) as compared to the Uni-O and No-flow groups ($p<0.05$) (Fig. 3a,b). Unidirectional laminar flows resulted in increased cell areas, whereas unidirectional oscillatory flows reduced the cell area by ~39.3%. There were, however, no significant differences in nuclear areas in the Uni-L (230.23±23.95 μm^2) and Uni-O (267.79±29.94 μm^2) groups (Fig. 2e). Nuclear areas were significantly higher for the Bi-O

group (387.74±74.33 μm^2) compared to other groups. Cells in the Uni-L group also showed significantly higher cytoskeletal/ nuclear area ratios (11.12±2.50), followed by No-flow (7.22±1.06), Bi-O (5.83±1.38), and Uni-O (3.50±0.60) groups (Fig. 2f). These results demonstrate that HAEC responds to the fluid shear stress to alter cell and nuclear morphologies *via* cytoplasmic remodeling. Flow induced shear stress on HAEC monolayers, hence, shape distinct changes in endothelial morphologies.

E-cadherin disruptions are augmented in monolayers under bidirectional oscillatory flows

Intercellular junctions regulate the transport of biomolecules across endothelial monolayers. Endothelial barrier function due to bacterial/ viral infections, inflammation, cancers, diabetes, atherosclerosis, and other diseases is maintained by junctional proteins[27]. VE-cadherin-mediated contacts and VEGF-R2 complexes, including PECAM, are critical transducers of the shear stresses exerted on the endothelial cell (EC) monolayer[28]. We used immunofluorescence methods to investigate changes in cell-cell adhesions with VE-cadherin and stress fiber (SF) formation under shear (see Methods).

Representative confocal images (Fig. 3a) show clear differences in VE-cadherin in monolayers subjected to laminar flow (Uni-L) as compared to other groups. VE-cadherin was stained continuously at the cell borders in the Uni-L group, whereas the Bi-O group showed discontinuous VE-cadherin expression. These results demonstrate the redistribution of gap junctions and cytoskeletal proteins that may compromise the monolayer integrity and increase membrane permeability. There was little VE-cadherin fluorescence intensity in the Uni-O and control (No-flow) groups, respectively. Monolayers in the Bi-O group had higher VE-cadherin compared to those in the Uni-O group. The extent of VE-cadherin expression change, shown in the XZ sectional image at a point marked for each of the representative images, demonstrates

differences in monolayer heights under oscillatory flows, No-flow, and Uni-L conditions (Fig. 3b, c). Fig. 3d also shows well-defined SF under unidirectional laminar flows.

We used these images to quantify actin intensities in monolayers subjected to various flow conditions. Actin was highest for the Uni-L (32.72±3.03 A.U.), followed by Bi-O (18.60±3.35 A.U.), No-flow (18.19±1.39 A.U.), and Uni-O groups (21.51±1.83 A.U.), respectively (Fig. 3e). There were significant differences in actin for the Bi-O group as compared to the Uni-O group ($p<0.05$). VE-cadherin expression was higher in the Uni-L group (32.72±3.03 A.U.) as compared to all other groups (Fig. 3f). The expression of VE-cadherin was lowest for the Uni-O group (15.46±0.97 A.U.) and was partially lower in the Bi-O (22.19±1.20 A.U.) group. There were no significant differences in VE-cadherin expressions between No-flow (17.99±2.41 A.U.) and Uni-O groups (Fig. 3f). These results show that secondary flows alter SF organization, nuclear sizes, and cell-cell junctional proteins that can impact monolayer integrity and barrier function.

Nuclear membrane disruptions, heterochromatin condensation, and gene expression changes under oscillatory flows

Cellular nuclei, the organization of chromatin, and transduction are regulated by mechanical forces[29,30]. We investigated possible changes in nuclear membrane proteins and chromatin organization in cell monolayers exposed to different flow conditions. Representative DAPI stained images (Fig. 4a) demonstrate distinct differences in the organization of heterochromatin structures, visible as multiple bright spots, in Bi-O monolayers compared to homogenous nuclear staining in other groups. Nuclear areas in Bi-O cells were 68.41% higher compared to No-flow (Fig. 3c).

The nuclear lamina plays a crucial role in the bidirectional transmission of forces between the cytoskeleton and the nucleus[31]. We tested changes in lamins localization under the

various shear conditions in our experiments. Lamin A/C acts as a scaffold for heterochromatin and other transcriptional proteins, and is critical in preventing force induced DNA damage[32]. Immunofluorescence staining shows distinct disruption and mislocalization of lamin A/C (Fig. 4b) from the membrane to the interior in HAEC monolayers subjected to oscillatory flows. In contrast, cells in No-flow and Uni-L groups show lamin A/C localization at the nuclear envelope. We divided the nuclear boundary into three concentric regions (R1, R2, and R3) of equal areas to quantify the sub-nuclear localization of lamin A/C (Fig. 4c). Results show lamin localization to the nuclear membrane for No-flow and Uni-L conditions (Fig. 4d). However, lamin intensity was 16.8 times higher in the R2 and R3 regions for cells in the Bi-O group, and 10.9 times higher for the Uni-O group as compared to Uni-L. Loss of lamin under oscillatory flows correlated with chromatin condensation in the cells (Fig. 4a). Disruption and mis-localization of lamin A/C may contribute to chromatin condensation and potentially impact cellular responses to flow.

We next asked if there were alterations to the gene expression levels in the monolayers under flow. We used PCR to analyze the regulation of mRNA levels for Actin, VE-Cadherin, NFκB, and LMNA genes in the flow groups and compared results with corresponding values in the No-flow group (Fig. 5). Results show increased NFκB and lamin A/C expression under oscillatory flows. Bi-O cells had 3.76±0.42 fold upregulation in inflammatory NFκB gene expression as compared to other groups. However, NFκB expression was downregulated in the Uni-L group (0.62±0.36), which suggests the importance of laminar unidirectional flows that result in anti-inflammatory properties. LMNA gene expression was also highly upregulated in the Bi-O (2.29±0.76) group, as well as actin in the Uni-L group (6.85±1.45). These data agree with immunofluorescence data in our study (Fig. 4b). We note a higher fold change in VE-Cadherin expression for the Uni-L group (5.29±1.09) relative to Bi-O (2.01±0.63) and Uni-O (1.31±0.44) conditions. Laminar flows hence enhance cell-cell junctional protein gene

expression in HAEC monolayers. Changes to lamins A/C, heterochromatin condensation, and increased inflammation due to secondary flows *via* changes to the cytoskeletal and nuclear mechanobiology have not been reported in endothelial studies. These results may have implications for understanding the cellular responses to shear stress and the development of vascular diseases.

Discussion

Mechanical forces are critical regulators of vascular biochemistry, gene expression, and homeostasis in endothelial monolayers[1,33]. The primary goal of our study was to fabricate an endothelium-on-chip device to generate controlled disturbed flows, and investigate the effects of complex flows on endothelial mechanobiology. Our work has four main implications. First, we developed a robust method to generate bidirectional oscillatory flows in a microfluidic device to replicate shear rosettes that characterize disturbed flows. The semi-analytical method computes inlet velocities to pumps in the device and generates any rosette shape. We demonstrate a good match between CFD and flow visualization studies that validate the model. This approach can be used to generate complex rosettes reported in disease prone arterial regions[11]. Second, we subjected HAEC monolayers to a circular shear rosette of 1Pa WSS magnitude, and compared morphological cellular changes with those subjected to laminar unidirectional and oscillatory flows. Immunofluorescence studies show distinct differences in EC morphologies and actin intensities due to flow. HAEC had higher areas, were cuboidal in shape, and had significantly larger nuclei in the Bi-O group than those in other groups. SF and VE-cadherins were clearly visible under Uni-L flows compared to cells in oscillatory flows that showed reduced fluorescence levels. Third, we observed disruption in lamin A/C and reorganization of heterochromatin in the nuclei for cells in the Bi-O group; these changes were not visible in Uni-L and No-flow conditions. Finally, we measured changes in the gene

expression levels and demonstrated significantly elevated actin, VE-cadherin, NF-kB, and lamin expression in cells from the Bi-O group that have not been reported earlier.

Various methods have been used to produce disturbed flows; these include naturally occurring or surgical interventions in animal models, vertical step flow chambers, modified cone-plate viscometers, and microfluidic systems to elucidate the phenotypic adaptation of cells to flow[8]. Animal models for atherosclerosis often involve partial ligation of arteries that alter flows and cause changes in cellular behaviors from atheroprotective to atheroprone in ligated regions[34]. Studies suggest the inclusion of substrate stretching with unidirectional laminar flows to better represent the *in vivo* cellular milieu[35,36]. Assays that preserve the physiological complexity are clearly warranted but present challenges due to limited access to imaging at cellular and sub-cellular levels. Developing therapeutics to manage and mitigate vascular disease is a continuing exercise due to the high costs for animal studies in screening novel compounds. There is a need for lab-on-chip platforms that accurately capture the complex biomechanical milieu to test a vast repertoire of flow conditions that are relevant in vascular disease. Such devices can provide accurate, efficient, and reliable results to decrease the exorbitant costs of animal trials and provide solutions for personalized medicine for a variety of genetic conditions. The device in this study represents a significant advance in this direction and provides a simple, versatile, inexpensive, and robust method to generate controlled disturbed flows. The semi-analytical model can be used to generate any arbitrary rosette at the device centroid, to potentially simulate flow patterns observed in diseased arteries.

We show flow-induced changes in endothelial morphologies using our device. Cellular shapes and actin cytoskeleton are clearly different at branch points of the aorta that undergo disturbed blood flows[18]. EC modify their morphology and orientation in response to the flows[24]. The cells under laminar flows in our study had elongated morphologies, and high actin

intensity with well-formed SF as compared to those subjected to oscillatory flows that were cuboidal without well-aligned SFs. PCR studies show significant upregulation in actin expression in cells from the Bi-O group as compared to other groups. VE-cadherin fluorescence was highest for the Uni-L group compared to all other groups (Fig. 2d). Earlier studies have also demonstrated reduced permeability under laminar shear stress due to the presence of tight adherens junctions[37]. In contrast, unidirectional oscillatory flows significantly lowered VE-cadherin, whereas bidirectional oscillatory flows showed partial downregulation. Disruption and reduction in VE-cadherin expression suggest a possible redistribution of gap junctions and cytoskeletal proteins that can compromise the monolayer integrity and increase the membrane permeability[21]. Reduction in membrane-bound VE-cadherin at disturbed flow regions leads to vascular destabilization, intercellular gap opening, loss of barrier function, and consequently enhanced macromolecular permeability[8,38].

Our results also show a remarkable increase in the nuclear areas of cells under bidirectional oscillatory flows (68.41%) compared to the No-flow group – these data suggest changes to the nuclear mechanotransduction. Heterochromatin condensation was significantly higher in cells from the Bi-O group as compared to all other groups (Fig. 4a). These cells also showed disruption and mislocalization of lamin A/C from the membrane to the nuclear interior. In contrast, cells in the No-flow and Uni-L flow conditions demonstrate lamin A/C localization at the nuclear envelope (Fig. 4b). Because the lamina is physically connected to the cytoskeleton through transmembrane LINC complex, and transmits forces from the cytoskeleton to the nucleoplasm, it plays a crucial role in cellular mechanotransduction[24]. The role of the nuclear lamina in endothelial mechanotransduction under differential shear stresses is poorly understood. A quantification of the extent of disruption of lamin expression can provide insights into the morphological and physiological implications of cellular responses to complex flows.

PCR analysis to quantify mechanotransduction showed increased NFκB upregulation in the Bi-O group, whereas unidirectional laminar flows resulted in its downregulation. NFκB is pro-inflammatory and is implicated in many vascular diseases, such as atherosclerosis and atherothrombosis[39]. Activation of NF-κB triggers other inflammatory mediators that modulate smooth muscle cell activation, which can further contribute to inflammation and atherosclerosis progression *in vivo*[40,41]. Our results agree with other studies that demonstrate increased inflammation in EC monolayers subjected to fluid flows acting perpendicular to aligned cells compared to those along the aligned monolayer direction that are anti-inflammatory and contribute to atheroprotection[41]. The increased expression of inflammatory genes in response to complex flows in our study also agrees with *in vivo* studies[7]. Inflammatory markers are also associated with phosphorylation of Lamin A/C and a loss of the nuclear lamina[31]. The significant upregulation in LMNA gene expression in Bi-O specimens in our study may be a compensatory mechanism for the reduced Lamin A/C at the nuclear lamina, which requires further investigation. Together, these results demonstrate the ability of the endothelium-on-chip device to assess the effects of disturbed flows on endothelial mechanobiology, provides unique potential to evaluate mechanosensory pathways implicated in conditions such as diabetes, and to test therapeutics that target vascular dysfunction.

Methods

Development of a semi-analytical model to calculate flow velocities in the endothelium-on-chip device to generate controlled disturbed flows

The microfluidic endothelium-on-chip device consists of three arms with an angular separation of 120º that resembles the Greek symbol λ (Fig. 1c). The device can produce any shape of the WSS rosette which represents a polar plot of the temporal variations in WSS vectors at each location on the surface[23]. We prescribe the shape of a targeted shear rosette at

the device centroid. This rosette may be regular, such as a circular or elliptical shape, or have complex shapes as that reported in diseased vessels[11]. We use a laminar and quasi-steady assumption to compute the flow rates into the inlets of the device using a semi-analytical model. In this method, we use the centroid of the device as the origin of the coordinate system (Fig. 1c). Based on the flow rates to the two pumps, we obtain the flow velocities at each of the two inlets, labeled V_1 and V_2, as

$$V_1 = V_0 \cos(\eta) \quad and \quad V_2 = V_0 \sin(\eta) \tag{2}$$

V_o is the amplitude, and η is the phase angle of the inlet velocity in the device. For fully developed flows, the components of the WSS vectors at the device centroid are given in terms of the dynamic viscosity, μ, the channel height, h, and the mean flow velocity components in the X and Y directions, $V_{X|C}$ and $V_{Y|C}$as

$$WSS_X = \frac{6\mu\overline{V_{X|C}}}{h} \quad and \quad WSS_Y = \frac{6\mu\overline{V_{Y|C}}}{h} \tag{3}$$

These mean flow velocities at the device centroid are calculated using the inlet velocities from the continuity equation as

$$\overline{V_{X|C}} = \frac{V_X}{C_X} \quad \text{and} \quad \overline{V_{Y|C}} = \frac{V_Y}{C_Y} \quad \text{and} \tag{4}$$

$C_X$and C_Y are channel-specific coefficients, which are essential to compute the increase in area at the centroidal region as compared to the areas at the inlet ports connected to the syringe pumps. For the device geometry fabricated in this study, $C_X = 15$ and $C_Y = 14$. Other geometries will result in different values of C_X and C_Y in these equations. V_X and V_Y are the X and Y components of the resultant velocities that are obtained by vectorially adding the inlet velocities, V_1 and V_2.

The ratio of WSS components at the centroid is written in terms of the phase angle of the inlet velocity in the device, η, by substituting equations (2) and (4) in (3) as

$$\frac{WSS_X}{WSS_Y} = \left(\frac{C_Y}{C_X} \; \frac{cos(\eta) - \sin(\eta)}{cos(\eta) + \sin(\eta)} \; \frac{1}{\tan\left(\frac{\pi}{3}\right)} \right) \tag{5}$$

The magnitude of velocity, V_o , is written from equation (4) by substituting $\overline{V_{X|C}}$ in the expression for WSS_X, is

$$V_0 = \frac{h\, WSS_X}{6\mu} \frac{C_X}{(\cos(\eta) - \sin(\eta)) \cos\left(\frac{\pi}{3}\right)} \tag{6}$$

These equations are used to calculate the velocity inputs to obtain any targeted rosette shape in the device with values of WSS_X and WSS_Y and known area increment coefficients. V_0 and η may be calculated at each time instant, t, using equations (5) and (6). We use these expressions in equation (2) to calculate the inlet velocities at the syringe pumps using the 'sum of sine fit' and obtain variations in V_1 and V_2 with time. For the circular rosette (Fig. 1d), with a WSS magnitude of 1 Pa, the predicted $V_1 = V_1(t)$ and $V_2 = V_2(t)$ are given using equations (1). WSS magnitude of 1 Pa represents the physiological shear stresses experienced by endothelial cells due to blood flows[11].

We used a commercial computational fluid dynamics solver (ANSYS-Fluent, 2020 R1) to simulate unsteady, viscous, and laminar flows in the channel using velocity inputs to the pump given by the semi-analytical model (Equation 1) for a circular rosette. The CFD model uses pressure-velocity coupling with laminar flow conditions and a first-order implicit method to discretize the time-step at 1 ms (Fig. S1). Spatial discretization of the convection and gradient terms was performed using the 2nd order upwind and least square cell-based methods, respectively. The residual criteria for three velocity components and mass conservation were set to 1E-04. A mesh resolution of 10 cells along the height direction was selected from grid independence studies (Fig. S2 and Table T1). 21,12,370 elements were included in the device geometry. Fluid density, $\rho = 1055$ kg/m^3, and dynamic viscosity, $\mu = 0.004$ kg/ms, were

used in these computations. Wall boundary conditions were implemented on all microchannel surfaces to connect both inlets to the outlet of the device. A pressure outlet boundary condition was used for the reservoir. Post-processing was performed using Paraview software.

WSS variations in the device were obtained from CFD simulations, and the results were compared with the semi-analytical model to validate this method. We calculated the Anisotropy Ratios, AR, at each wall node in the device geometry to generate contour plots from the CFD analysis for each of the different targeted shear rosettes. The contour plots allowed us to visualize and understand the distribution of AR values across the device. This validation is central in studying the effects of complex flow conditions on endothelial morphology, signaling, and transduction responses.

Fabrication and validation of microfluidic devices to generate controlled flows

We used a replica molding technique to prepare microfluidic devices in this study using chemically etched stainless sheets (100 µm). In this method, we attached an etched sheet to a glass slide treated with trichloro silane (1H,1H,2H,2H-perfluorooctyl; Sigma Aldrich, India) in a desiccator overnight to prevent adhesion of polydimethylsiloxane (PDMS; Sylgard®184, Dow Corning, USA). PDMS was mixed in a stoichiometric ratio of 10:1 based on the manufacturer's instructions, poured over the prepared channel geometries, degassed to remove air bubbles, cured at 80°C for 2 hours, and peeled carefully to obtain the microfluidic channels. The channel height was 100 µm, and the width of the cross-sections in the three arms was 200 µm. We used a similar procedure to fabricate straight microfluidic channels using laser-cut acrylic tape with dimensions of 10 mm length X 1mm width X 100µm height for experiments using unidirectional and oscillatory flows. Inlet and outlet holes were punched using a 0.5 mm biopsy punch; the devices were cleaned and sterilized with 100% ethanol for cell culture experiments.

Two synchronized syringe pumps allow liquid at desired flow rates, derived for the specific rosette shape as described earlier, into the device and produce oscillatory or steady flows within the central region of the device. The third arm of the microfluidic channel in the device is connected to a reservoir. Absence of moving parts makes the device robust in utility, durability, and replicability. Molded PDMS parts were clamped to coverslips using a 3D-printed hollow frame to reduce lateral movement and visualize the device regions under an inverted microscope during the experiment. The frame was pressed down by four screws to apply uniform pressure on the PDMS channel and coverslip, and prevent leaks during the flow experiments[23]. The frame was dismantled at the end of the flow experiment to fix the cells on the coverslip.

We compared computationally obtained streamlines in the device for the circular rosette with streak images obtained in flow visualization experiments in which 0.1% v/v green fluorescent 2 µm sized polystyrene beads in MilliQ water were used as tracers (Movie3). Beads were first injected into the channel area, and the flow was visualized after a settling time of 15 minutes with the injection of bead solution from the pumps. Images were captured on the Leica SP5 epifluorescence system at 25 frames per second. The streak images indicate streamlines that closely match with streamlines obtained using computation.

Cell Culture and Seeding

Human aortic endothelial cells (HAECs) were purchased from LONZA (Lonza cat. no. CC-2535) and used at early passages of 2 to 5 in all experiments in this study. Cells were cultured in EGM™-2 Endothelial Cell Growth Medium-2 BulletKit (Lonza cat. no. CC-3162) in sterile conditions within a 5% CO_2 and 37°C incubator. Glass coverslips (22 mm) were cleaned using ultrasonication, activated using oxygen plasma for 2 minutes, and coated with

40 μg/ml of rat tail collagen-1 (A1048301, Thermo) at 37°C for 1 hour in a humid chamber. Prepared coverslips were washed three times with phosphate-buffered saline (PBS, Thermo) and seeded with HAECs at 1×10^6 cell/mL density to produce a ~90%confluent EC monolayer in 48 hours.

The PDMS channel was placed on the coverslip with the HAEC monolayer, and the channel was press-fit using a frame. This method differs from other studies, which takes a significantly long time to prepare channels with confluent endothelial cells for flow studies[23]. This older procedure involves flowing a small volume of media with endothelial cells into microfluidic channels, waiting for cell attachment and monolayer confluency within the chamber. The press-fit technique is relatively easy and saves preparation time for experiments. We used programmable syringe pumps (NE-1000, Syringepump.com) that were synchronized using an RS-232 dual pump communications cable for bidirectional oscillatory (Bi-O) flow studies. In this method, one pump serves as the Master control pump and the other as the secondary slave. Inlet flow rates from equation (1) were calculated for various time points over the entire cycle and input to the two pumps. Experiments on unidirectional laminar (Uni-L) and oscillatory (Uni-O) experiments were performed for 24 hours using a single pump with a duty cycle similar to the Bi-O studies.

Immunofluorescence

Cells were washed with PBS buffer (Fisher Scientific), fixed with 4% paraformaldehyde for 15 minutes, permeabilized with 0.1% Triton X-100 for 3 minutes, and blocked in 5% BSA + 5%FBS for 1 hour at room temperature. Samples were incubated for 1 hour at room temperature in primary antibody for VE-Cadherin (1:500, 2158, CST), Lamin A/C (1:500, MA3-1000, Thermo), and secondary Alexa fluor 488 (Molecular Probes, Invitrogen) antibody with a dilution of 1:600 and Rhodamine-phalloidin (Invitrogen) with a

dilution of 1:200 for 1 hour at room temperature, and rinsed twice using PBS. Samples were treated with DAPI (1:500, Invitrogen) for 2 minutes, rinsed twice with PBS to label nuclei, and mounted on coverslips with Goldfade (Invitrogen). A Leica SP5 FALCON confocal microscope was used to image the samples. Cell areas and aspect ratios were quantified using the Tissue analyser (Fiji by ImageJ).

RNA Isolation and RT-QPCR

Cell monolayers were washed with PBS buffer (Fisher Scientific) and treated with 200 µl of TRIzol® reagent (ThermoScientific) per coverslip in a PDMS well of an internal diameter of 0.5mm placed on the device centroid to isolate the cells subjected to $0.6 \leq AR \leq 1.0$ for analysis in the bidirectional oscillatory shear condition. Cells subjected to laminar and oscillatory unidirectional groups were isolated and collected from the channels. RNase Mini Kit (Qiagen) was used per the manufacturer's instructions. 2 µg of RNA was used for cDNA synthesis using a high-capacity cDNA reverse transcription kit (Applied Biosystems). PCR products were checked using Quantitative real-time PCR (qRT-PCR) using a Power up SYBR Green master mix (ThermoScientific) with 10 ng of cDNA as the template. Gene expressions were normalized to GAPDH. Fold change was calculated using the 2-ΔΔct method and normalized again to Control (No-flow) monolayers. Gene expressions were analyzed across three biological replicates in this study.

Statistical analysis

Experiments were performed in three independent trials. Data are reported as mean ± SD. Results from the different groups were compared using a one-way analysis of variance (ANOVA) with Bonferroni comparison to test for individual differences. $p < 0.05$ is indicated with (*).

Acknowledgements

We thank the Bioimaging Facility, Division of Biological Sciences, IISc, for the use of the Lecia SP8 FALCON confocal microscope. We also acknowledge the early work by Mr. Vamsi Krishna, who had initiated this work. NG is grateful to DBT (Biodesign and Bioengineering) for project support.

Author contributions

Conceptualization: JHA, NG; Methodology: NP, SM, JHA, NG; Software & Modeling: SM; Validation: NP, SM; Formal Analysis: NP, SM, JHA, NG; Investigation: NP, SM; Data Curation: NG; Writing - Original Draft Preparation: NP, SM, NG; Writing - Review & Editing: NP, SM, JHA, NG; Visualisation: NP, SM, NG; Supervision: JHA, NG; Funding Acquisition: NG

Competing interests

All authors declare that they do not have any conflict of interest.

References

1. Fang, Y., Wu, D. & Birukov, K. G. Mechanosensing and mechanoregulation of endothelial cell functions. *Compr. Physiol.* 9, 873 (2019).
2. Galie, P. A. *et al.* Fluid shear stress threshold regulates angiogenic sprouting. *Proc. Natl. Acad. Sci. U. S. A.*111, 7968–7973 (2014).
3. Poduri A., Chang A. H., Raftrey B., Rhee S., Van M., Red-Horse K. Endothelial cells respond to the direction of mechanical stimuli through SMAD signaling to regulate coronary artery size. *Development*. 144(18): 3241-3252 (2017).
4. Souilhol, C. *et al.* Endothelial responses to shear stress in atherosclerosis: a novel role for developmental genes. *Nat. Rev. Cardiol. 171*17, 52–63 (2019).
5. Kwak, Brenda R et al. Biomechanical factors in atherosclerosis: mechanisms and clinical implications. *European Heart J.* 35 (43): 3013-20, 3020a-3020d(2014).
5. McDaniel, Michael C et al. Localization of culprit lesions in coronary arteries of patients with ST-segment elevation myocardial infarctions: relation to bifurcations and curvatures. *American Heart J.* 161 (3): 508-15 (2011).
6. Theofilis, P. *et al.* Inflammatory mechanisms contributing to endothelial dysfunction. *Biomed.* 9(*781*9): 781 (2021).
7. Brown, A. J. *et al.* Role of biomechanical forces in the natural history of coronary atherosclerosis. *Nat. Rev. Cardiol. 134*13, 210–220 (2016).
8. Chiu, J. J. & Chien, S. Effects of disturbed flow on vascular endothelium: pathophysiological basis and clinical perspectives. *Physiol. Rev.*91, 327–387 (2011).
9. Weinberg, P. D. Haemodynamic Wall Shear Stress, Endothelial Permeability and Atherosclerosis—A Triad of Controversy. *Front. Bioeng. Biotechnol.*10, (2022).
10. Soehnlein, O. & Libby, P. Targeting inflammation in atherosclerosis — from experimental insights to the clinic. *Nat. Rev. Drug Discov.* 20820: 589–610 (2021).

11. Krishna, C. V., Chandran S., V., Watton, P. N., Arakeri, J. H. & Gundiah, N. Shear stress rosettes capture the complex flow physics in diseased arteries. *J. Biomech.*104, 109721 (2020).

12. Krishna, C. V., Gundiah, N. & Arakeri, J. H. Separations and secondary structures due to unsteady flow in a curved pipe. *J. Fluid Mech.*815, 26–59 (2017).

13. Ohta, M. *et al.* A Review of Functional analysis of endothelial cells in flow chambers. *J. Funct. Biomater.*13, (2022).

14. Meng, F. *et al.* In vitro fluidic systems: Applying shear stress on endothelial cells. *Medicine in Novel Technology and Devices*, 15: 100143 (2022).

15. Kim, D. H., Pak, K. W., Park, J., Levchenko, A. & Sun, Y. Microengineered platforms for cell mechanobiology. *Annu. Rev. Biomed. Eng.*11: 203–233 (2009).

16. Doherty, E. L., Aw, W. Y., Hickey, A. J. & Polacheck, W. J. Microfluidic and organ-on-a-chip approaches to investigate cellular and microenvironmental contributions to cardiovascular function and pathology. *Front. Bioeng. Biotechnol.*9: 25 (2021).

17. Chien, S. Effects of disturbed flow on endothelial cells. *Ann. Biomed. Eng.*36, 554–562 (2008).

18. Tovar-Lopez, F. *et al.* A microfluidic system for studying the effects of disturbed flow on endothelial cells. *Front. Bioeng. Biotechnol.*7, (2019).

19. Balaguru, U. M. *et al.* Disturbed flow mediated modulation of shear forces on endothelial plane: A proposed model for studying endothelium around atherosclerotic plaques. *Sci. Rep.*6, (2016).

20. Warboys, C. M., Ghim, M. & Weinberg, P. D. Understanding mechanobiology in cultured endothelium: A review of the orbital shaker method. *Atherosclerosis* 285: 170–177 (2019).

21. Baeyens, N., Bandyopadhyay, C., Coon, B. G., Yun, S. & Schwartz, M. A. Endothelial

fluid shear stress sensing in vascular health and disease. *J. Clin. Invest.*126, 821–828 (2016).

22. Zhou, J., Li, Y. S. & Chien, S. Shear stress-initiated signaling and its regulation of endothelial function. *Arterioscler. Thromb. Vasc. Biol.*34(10):2191-8 (2014).

23. Indian Patent Application No. 202341005523- A microfluidic device for inducing bidirectional oscillatory shear stress on biological cells, Filing date: 27th January 2023.

24. Wang, C., Baker, B. M., Chen, C. S. & Schwartz, M. A. Endothelial cell sensing of flow direction. *Arterioscler. Thromb. Vasc. Biol.*33, 2130–2136 (2013).

25. Sorescu, G. P. *et al.* Bone morphogenic protein 4 produced in endothelial cells by oscillatory shear stress induces monocyte adhesion by stimulating reactive oxygen species production from a Nox1-based NADPH oxidase. *Circ. Res.*95, 773–779 (2004).

26. Bednarek, R. In vitro methods for measuring the permeability of cell monolayers. *Methods Protoc.*5(1):17 (2022).

27. Gavard, J. Endothelial permeability and VE-cadherin: a wacky comradeship. *Cell Adh. Migr.*7, 465–471 (2013).

28. Khatau, S. B. *et al.* A perinuclear actin cap regulates nuclear shape. *Proc. Natl. Acad. Sci. U. S. A.*106, 19017–19022 (2009).

29. Ramdas, N. M. & Shivashankar, G. V. Cytoskeletal control of nuclear morphology and chromatin organization. *J. Mol. Biol.*427, 695–706 (2015).

30. Dobrzynska, A., Gonzalo, S., Shanahan, C. & Askjaer, P. The nuclear lamina in health and disease. *Nucleus*7(3):233-48 (2016).

31. Nava, M. M. *et al.* Heterochromatin-driven nuclear softening protects the genome against mechanical stress-induced damage. *Cell* 181, 800-817.e22 (2020).

32. Chatterjee, S., Fujiwara, K., Pérez, N. G., Ushio-Fukai, M. & Fisher, A. B. Mechanosignaling in the vasculature: Emerging concepts in sensing, transduction and

physiological responses. *Am. J. Physiol. - Hear. Circ. Physiol.*308, H1451–H1462 (2015).

33. Nam, D. *et al.* Partial carotid ligation is a model of acutely induced disturbed flow, leading to rapid endothelial dysfunction and atherosclerosis. *Am. J. Physiol. - Hear. Circ. Physiol.*297, 1535–1543 (2009).

34. US20160046897A1 - Organ mimic device with microchannels and methods of use and manufacturing thereof - Google Patents. Available at: https://patents.google.com/patent/US20160046897A1/en.

35. WO2013086502A1 - Organ chips and uses thereof - Google Patents. Available at: https://patents.google.com/patent/WO2013086502A1/en.

36. Sedlak, J. M. & Clyne, A. M. A. Modified parallel plate flow chamber to study local endothelial response to recirculating disturbed flow. *J. Biomech. Eng.*142(4): 0410031-04100312 (2020).

37. Miao, H. *et al.* Effects of flow patterns on the localization and expression of VE-cadherin at vascular endothelial cell junctions: in vivo and in vitro investigations. *J. Vasc. Res.*42(1):77-89 (2005).

38. Janota, C. S., Calero-Cuenca, F. J. & Gomes, E. R. The role of the cell nucleus in mechanotransduction. *Curr. Opin. Cell Biol.*63, 204–211 (2020).

39. Cunningham, K. S. & Gotlieb, A. I. The role of shear stress in the pathogenesis of atherosclerosis. *Lab. Invest.* 85, 9–23 (2005).

40. Ghim, M. *et al.* Endothelial cells exposed to atheroprotective flow secrete follistatin-like 1 protein which reduces transcytosis and inflammation. *Atherosclerosis* 333: 56–66 (2021).

41. Kojok, K., El-Kadiry, A. E. H. & Merhi, Y. Role of NF-κB in platelet function. *Int. J. Mol. Sci.*20(17):4185 (2019).

List of Figures

Figure 1: Disturbed flow regions (maroon) in the **(a)** aortic arch and descending artery, and **(b)** arterial bifurcations experience secondary flows that correlate with atheroprone areas. **(c)** Endothelium-on-chip device shows the clamping frame for the replica molded PDMS channel, HAEC monolayer on a coverslip, two syringe pumps, and a reservoir. **(d)** Shear rosettes are polar plots that show variations in shear stresses over one cycle. The target of a circular rosette profile (blue) closely matches the rosette obtained from CFD using velocity input (magenta) from the model. **(e)** Inlet velocity profile for the two pumps obtained from the semi-analytical model was used to generate a circular shear rosette. **(f)** Contour plot shows AR variations for a circular rosette (AR=1) at the device centroid. **(g)** Matched target shear rosette (blue) for a point in the ICA with an aneurysm, is shown with the rosette obtained from CFD using velocity input from the analytical model (magenta)[11] **(h)** Velocities to the pump inlets were calculated using the semi-analytical model. **(i)** The AR contour map generated at the device centroid is shown using these flow inlets. **(j,l)** Transient streamlines from CFD calculations are shown at 205 ms and 505 ms **(k,m).** The corresponding streak images indicating streamlines obtained from flow visualization experiments are shown for comparison.

Figure 2: Changes in HAEC morphologies were clearly visible at 24 hours in response to flow oscillations and directions for **(a)** No-flow (Control), Uni-L, Uni-O, and Bi-O conditions. Actin was stained with Rhodamine phalloidin (red) and the nucleus with DAPI (blue). Scale bar 25µm. **(b)** Monolayers were segmented using TissueAnalyser (Fiji) to obtain individual cell areas that are clearly different under flow **(c)** Plots show differences in HAEC areas, **(d)** Aspect ratios, **(e)** Nucleus areas, and **(f)** Cell to nucleus area ratios for the different flow groups as compared to the Control condition. $p<0.05$ was considered statistically significant.

Figure 3:(a) HAEC monolayers were stained using VE-cadherin (green), actin (red), and nucleus (blue) in monolayers subjected to the various flow conditions. Apparent differences are visible in representative immunofluorescence images from these studies. Scale bar 25µm. **(b)** The VE-Cadherin intensity is clearly different in Uni-L flows as compared to the other groups. **(c)** The XZ image for this representative image is shown at a point labeled in (**b**) to demonstrate differential monolayer heights in response to flows. **(d)** 63x image of the monolayer shows differences in actin fluorescence and stress fibers in the HAEC monolayer for the various groups. Nuclei in the monolayer from the Bi-O group look significantly larger as compared to other groups. Scale bar 25 µm. **(e)** Immunofluorescence images were used to quantify the intensity of Actin (red) and **(f)** VE-cadherin in cell monolayers corresponding to the various groups in the study to demonstrate altered permeability. $p<0.05$ was considered statistically significant.

Figure 4: Immunofluorescence images of nuclei in the HAEC monolayers are shown in **(a)** blue (DAPI) for the various groups in the study. Size differences in nuclei in Uni-O and Bi-O flow conditions were clearly visible. Cells under oscillatory flows (Uni-O and Bi-O) show heterochromatin condensation **(b)** Lamin A/C staining in the nuclear lamina shows clear differences for the different flow conditions. Nuclear lamina disruption was visible under oscillatory flow (Uni-O, and Bi-O) conditions. **(c)** We used a graphical representation to quantify the differences in Lamin A/C redistribution within three regions of equal area in the nucleus. **(d)** Cells under oscillatory flow conditions (Uni-O and Bi-O) show lamin redistribution in the nucleus (25-30 cells in each group).

Figure 5: PCR quantification of mRNA fold change is shown for Actin, VE-Cadherin, NFκB, and LMNA genes for the various groups in the study. Fold change in each group was

normalized to GAPDH and No-flow conditions. Cells in the Bi-O group show elevated expression of all markers as compared to other groups.

Figure 1

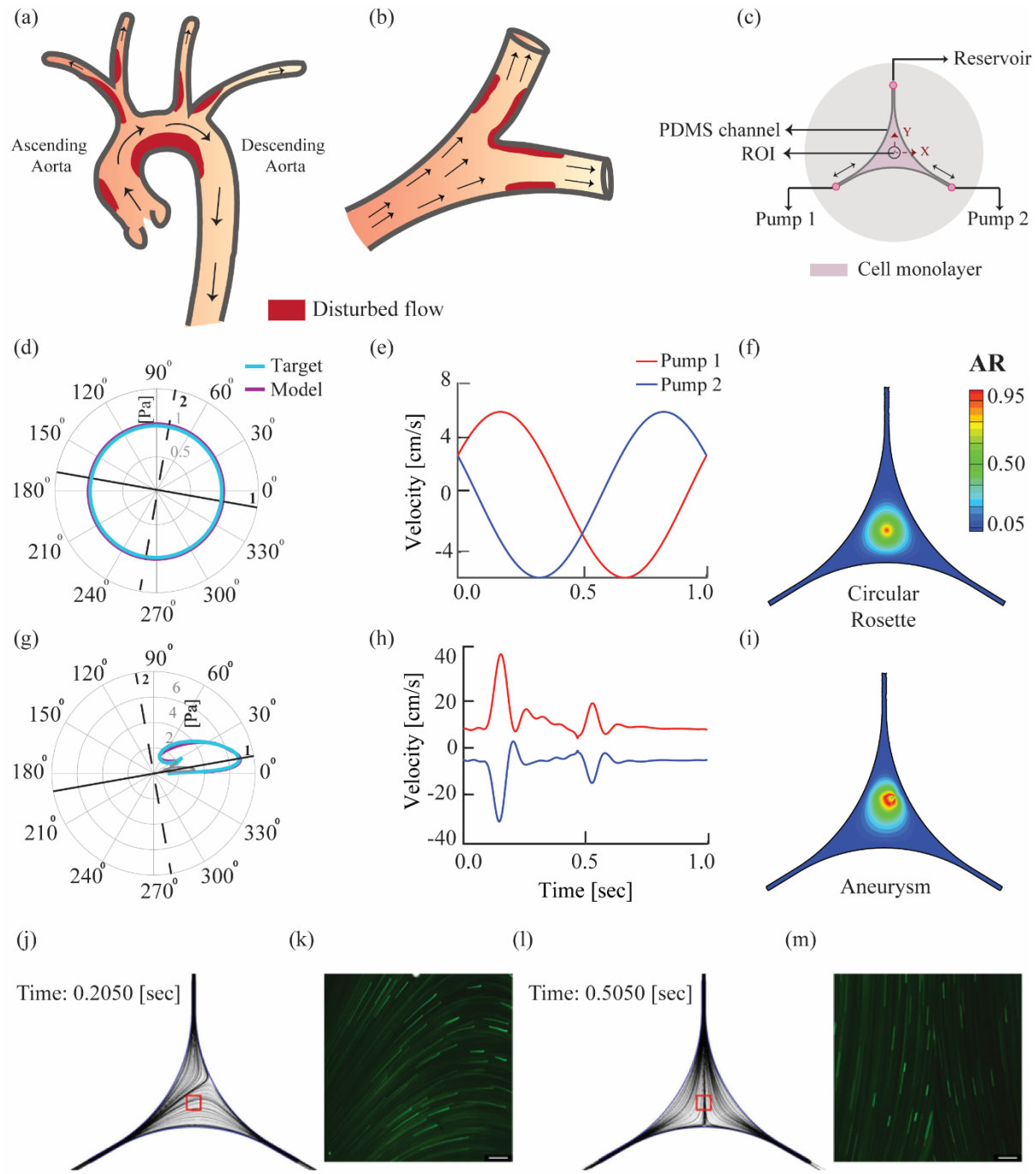
(a)
Ascending Aorta
Descending Aorta
Disturbed flow
(b)
(c)
Reservoir
PDMS channel
ROI
Pump 1
Pump 2
Cell monolayer
(d)
Target
Model
[Pa]
(e)
Pump 1
Pump 2
Velocity [cm/s]
(f)
AR
0.95
0.50
0.05
Circular Rosette
(g)
[Pa]
(h)
Velocity [cm/s]
Time [sec]
(i)
Aneurysm
(j)
(k)
(l)
(m)
Time: 0.2050 [sec]
Time: 0.5050 [sec]

Figure 2

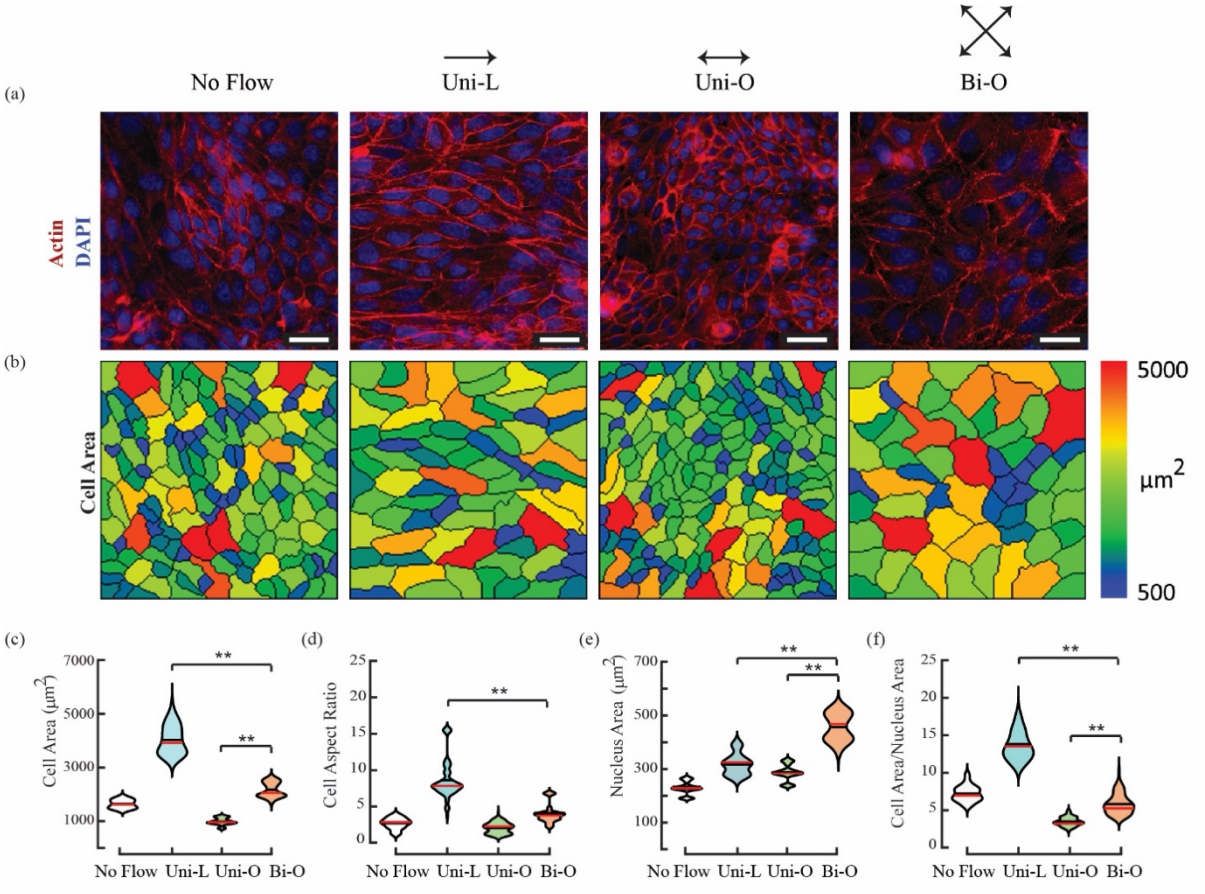
(a)
No Flow
Uni-L
Uni-O
Bi-O
Actin
DAPI
(b)
Cell Area
5000
μm2
500
(c)
Cell Area (μm2)
7000
5000
3000
1000
**
**
No Flow Uni-L Uni-O Bi-O
(d)
Cell Aspect Ratio
25
20
15
10
5
0
**
No Flow Uni-L Uni-O Bi-O
(e)
Nucleus Area (μm2)
700
500
300
100
**
**
No Flow Uni-L Uni-O Bi-O
(f)
Cell Area/Nucleus Area
25
20
15
10
5
0
**
**
No Flow Uni-L Uni-O Bi-O

Figure 3

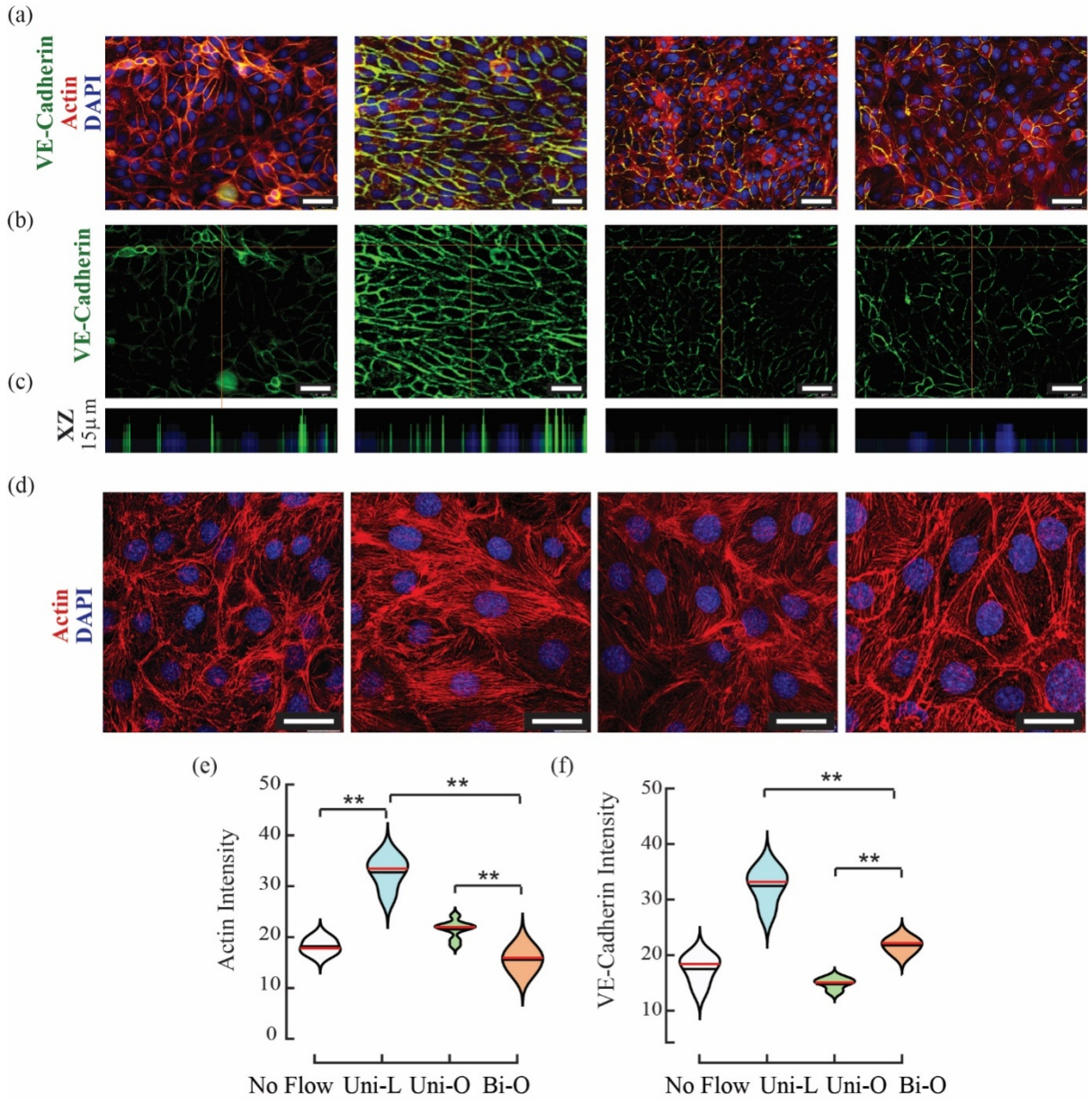
(a)
VE-Cadherin
Actin
DAPI
(b)
VE-Cadherin
(c)
XZ
15μm
(d)
Actin
DAPI
(e)
Actin Intensity
50
40
30
20
10
0
**
**
**
No Flow
Uni-L
Uni-O
Bi-O
(f)
VE-Cadherin Intensity
50
40
30
20
10
**
**
No Flow
Uni-L
Uni-O
Bi-O

Figure 4

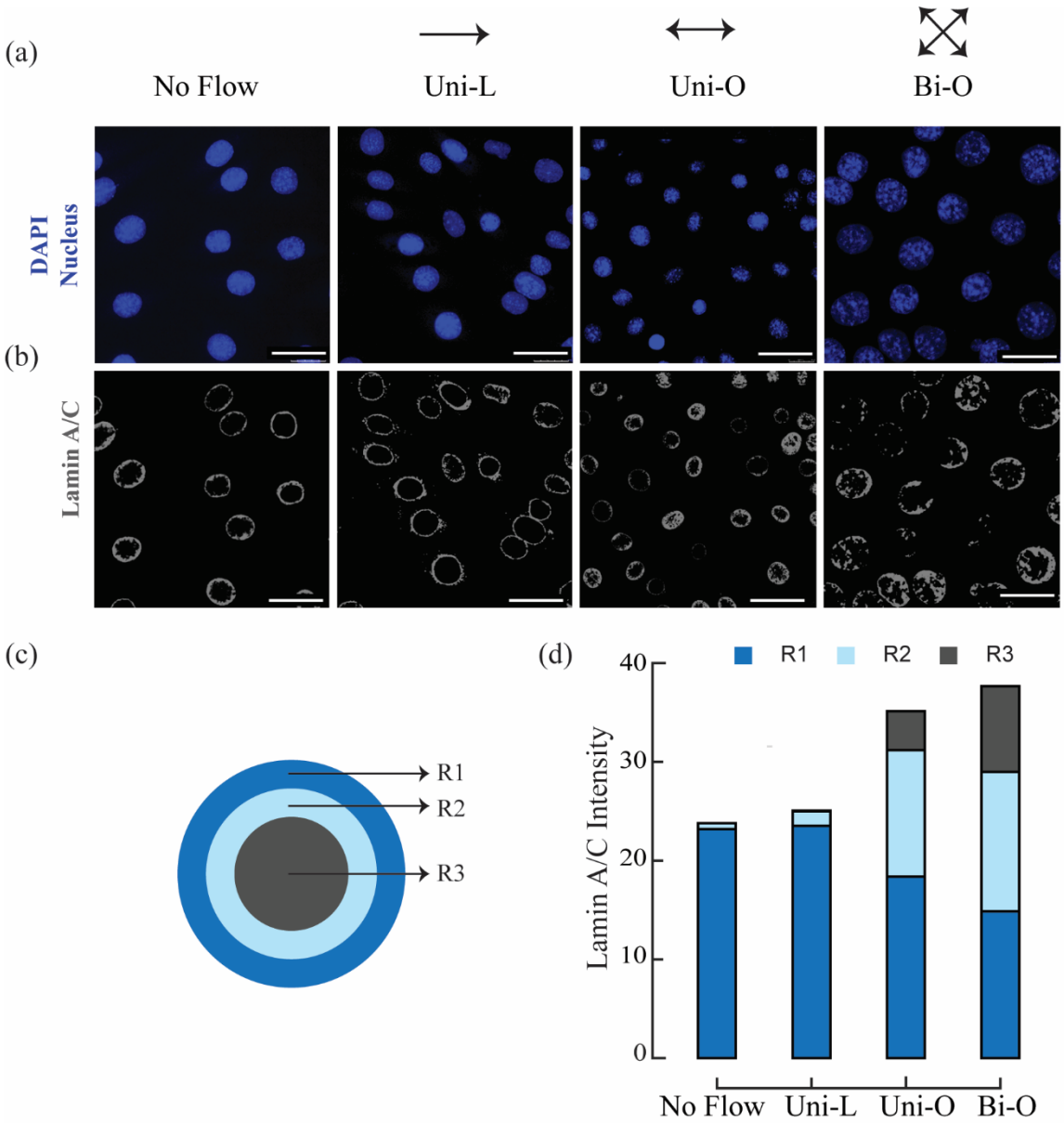
(a)
No Flow
Uni-L
Uni-O
Bi-O
DAPI
Nucleus
(b)
Lamin A/C
(c)
R1
R2
R3
(d)
R1
R2
R3
Lamin A/C Intensity
40
30
20
10
0
No Flow
Uni-L
Uni-O
Bi-O

Figure 5

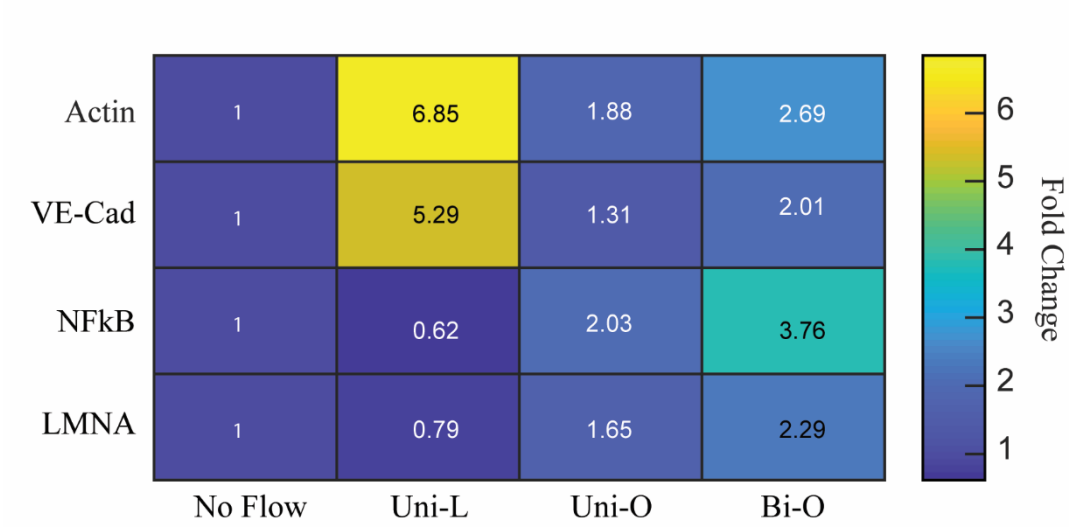
Actin
VE-Cad
NFkB
LMNA
1
6.85
1.88
2.69
1
5.29
1.31
2.01
1
0.62
2.03
3.76
1
0.79
1.65
2.29
No Flow
Uni-L
Uni-O
Bi-O
6
5
4
3
2
1
Fold Change

List of Supplementary Figures

Figure S1: X and Y components of the velocity profiles, shown in (**a**) and (**b**), were extracted at the centroid of the channel at 30 ms for the circular shear rosette. Due to the close match between the velocity profile for 1 ms and 0.1 ms, we chose a higher time step of 1 ms for the final computations. WSS magnitude at the centroid of the channel is constant for the time step of 1 ms and 0.1 ms (Table T2).

Figure S2: To assess mesh independence, we used 5, 7, and 10 cells across the height of the channel and plotted the X and Y components of the velocity in (a) and (b) subplots for all cases. Velocities were extracted at the centroid of the channel at 300 ms for the circular shear rosette. The mesh resolution of 10 cells shows comparatively smooth velocity profiles. Hence, we used it for the final computations. In this study, WSS is a prime quantity analyzed using computational data. Its magnitude at the centroid of the channel is almost constant for the mesh resolution of 7 cells and 10 cells (Table T1).

Figure S3: (a) Our semi-analytical model can be used to generate any shape of the shear rosette to characterize regions of disturbed flow. Results show a close match between the targeted rosette reported for aortic aneurysmal (AA) regions[11] and the computationally obtained rosette at the centroid of the channel using the velocity input predicted by the semi-analytical model. (b) Velocity profiles from the semi-analytical model that served as input to syringe pumps in the endothelium-on-chip device. (c) Contour plots show AR distributions for the AA rosette. (d) Results are also demonstrated for an elliptical rosette of magnitude 1 Pa using the semi-analytical model that closely matches results from the semi-analytical model. (e) Velocity

inputs to generate the elliptical rosette serve as inputs to the two syringe pumps. (f) corresponding AR distributions are shown for the elliptical rosette.

Figure S1

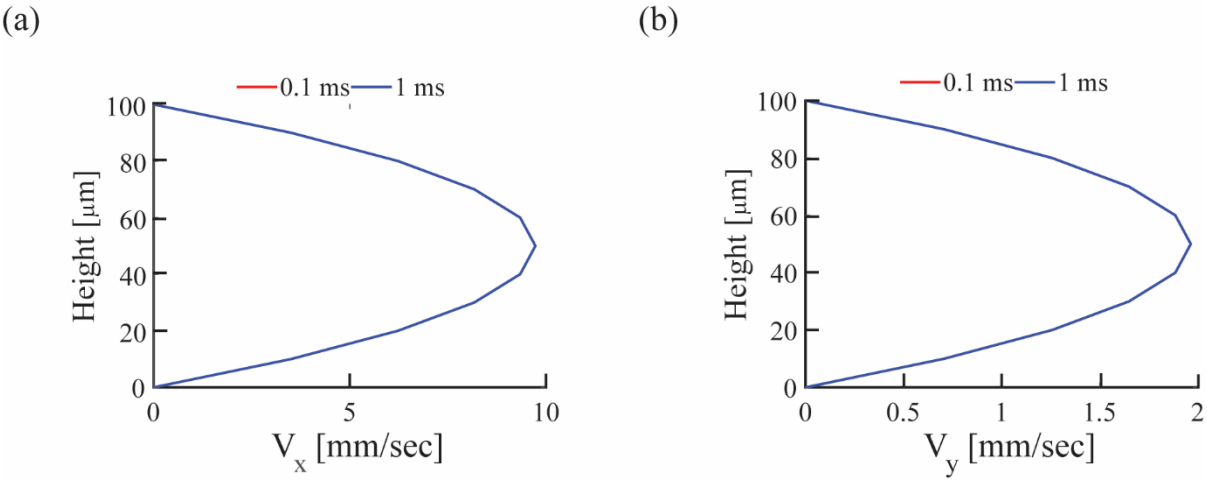
(a)
0.1 ms
1 ms
Height [μm]
100
80
60
40
20
0
0
5
10
Vx [mm/sec]
(b)
0.1 ms
1 ms
Height [μm]
100
80
60
40
20
0
0
0.5
1
1.5
2
Vy [mm/sec]

Figure S2

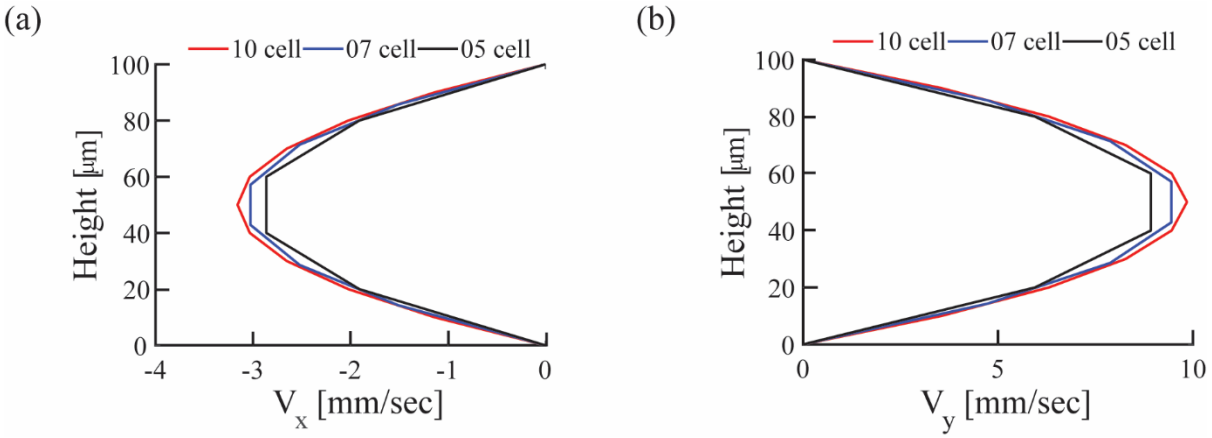
(a)
10 cell
07 cell
05 cell
Height [µm]
100
80
60
40
20
0
-4
-3
-2
-1
0
Vx [mm/sec]
(b)
10 cell
07 cell
05 cell
Height [µm]
100
80
60
40
20
0
0
5
10
Vy [mm/sec]

Figure S3

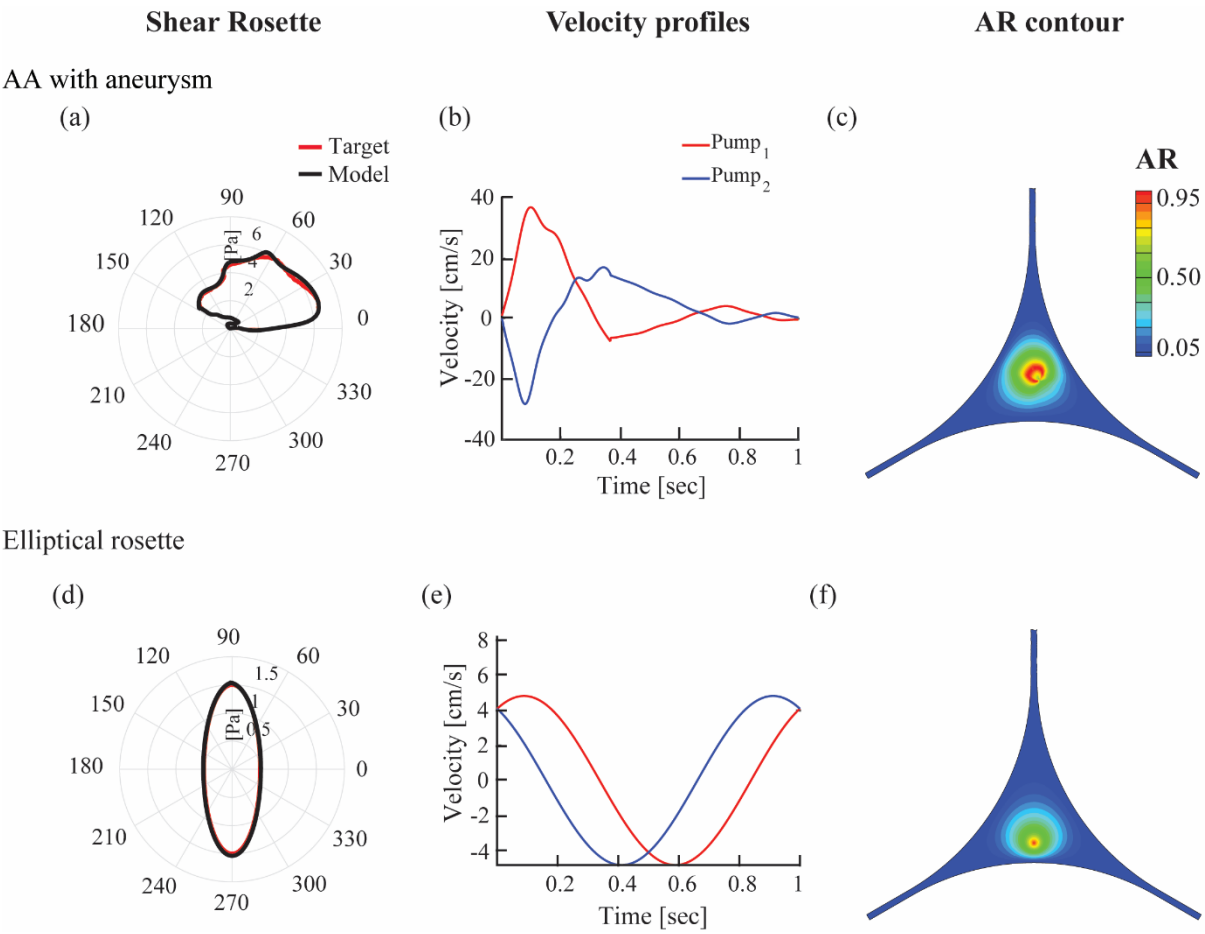
Shear Rosette
Velocity profiles
AR contour
AA with aneurysm
(a)
Target
Model
[Pa]
(b)
Pump1
Pump2
Velocity [cm/s]
Time [sec]
(c)
AR
0.95
0.50
0.05
Elliptical rosette
(d)
[Pa]
(e)
Velocity [cm/s]
Time [sec]
(f)

List of Supplementary Tables

Table T1: Mesh independence study: size

No. of cells along the height	05	07	10
Minimum cell size [μm]	20	15	10
|WSS| [Pa]	1.91	1.99	2.03

Table T2: Time step selection

	WSS [Pa]	
T[Sec]	**[dt=0.1mSec]**	**[dt=1mSec]**
0.02	1.94	1.94
0.03	1.95	1.95

List of Supplementary Movies

Movie 1: The velocity inputs provided to the two pumps connected to the inlet ports of the endothelium-on-chip device, along with the corresponding wall shear stress (WSS) values on the shear rosette map, are illustrated. These inputs were employed to generate a circular rosette pattern at the centroid of the device.

Movie 2: The velocity inputs and corresponding WSS variations in the endothelium-on-chip device are illustrated for a shear rosette pattern corresponding to an internal carotid artery (ICA) with an aneurysm[11] reported in an earlier study.

Movie 3: Results comparing computationally derived streamlines depicting fluid flows in the endothelium-on-chip device with streak images obtained from experimental flow visualization, performed with 2 μm tracer beads suspended in the fluid, demonstrate a close match in a region shown with a box in the device.